CONDENSED MATTER PHYSICS

First demonstration of tuning between the Kitaev and Ising limits in a honeycomb lattice

Faranak Bahrami[1], Xiaodong Hu[1], Yonghua Du[2], Oleg I. Lebedev[3], Chennan Wang[4], Hubertus Luetkens[4], Gilberto Fabbris[5], Michael J. Graf[1], Daniel Haskel[5], Ying Ran[1], Fazel Tafti[1]*

Recent observations of novel spin-orbit coupled states have generated interest in 4*d*/5*d* transition metal systems. A prime example is the $J_{\text{eff}} = \frac{1}{2}$ state in iridate materials and α-$RuCl_3$ that drives Kitaev interactions. Here, by tuning the competition between spin-orbit interaction (λ_{SOC}) and trigonal crystal field (Δ_T), we restructure the spin-orbital wave functions into a previously unobserved $\mu = \frac{1}{2}$ state that drives Ising interactions. This is done via a topochemical reaction that converts Li_2RhO_3 to $Ag_3LiRh_2O_6$. Using perturbation theory, we present an explicit expression for the $\mu = \frac{1}{2}$ state in the limit $\Delta_T \gg \lambda_{SOC}$ realized in $Ag_3LiRh_2O_6$, different from the conventional $J_{\text{eff}} = \frac{1}{2}$ state in the limit $\lambda_{SOC} \gg \Delta_T$ realized in Li_2RhO_3. The change of ground state is followed by a marked change of magnetism from a 6 K spin-glass in Li_2RhO_3 to a 94 K antiferromagnet in $Ag_3LiRh_2O_6$.

INTRODUCTION

An exotic quantum state in condensed matter physics is the $J_{\text{eff}} = \frac{1}{2}$ state in honeycomb iridate materials that leads to the Kitaev exchange interaction (*1*–*6*). The $J_{\text{eff}} = \frac{1}{2}$ state is a product of strong spin-orbit coupling (SOC) in heavy Ir^{4+} ions that splits the t_{2g} manifold into a $J_{\text{eff}} = \frac{3}{2}$ quartet and a $J_{\text{eff}} = \frac{1}{2}$ doublet. With five electrons in the $5d^5$ configuration, iridates have one electron in the spin-orbital $J_{\text{eff}} = \frac{1}{2}$ state that satisfies the prerequisites of the Kitaev interaction in a honeycomb lattice as shown by earlier studies (*1*–*5*). Here, we introduce a new spin-orbital state, $\mu = \frac{1}{2}$, which we have engineered by tuning the interplay between two energy scales: the SOC (λ_{SOC}) and the trigonal crystal field splitting (Δ_T). The $\mu = \frac{1}{2}$ state drives Ising instead of Kitaev interactions. Although the Ising limit has been discussed in several theoretical studies (*7*–*10*), a transition between the Kitaev and Ising limits has not been demonstrated until now. It has been theoretically predicted that the Kitaev limit in Na_2IrO_3 can be tuned to an Ising limit under uniaxial physical pressure (*8*), but the required pressure has not been achieved. The Ising limit is relevant to MPS_3 (*M* = Mn, Fe, and Ni) compounds (*10*); however, a transition from the Ising to Kitaev limit has not been discussed in those materials, even at a theoretical level. This work presents the first observation of a transition between the Kitaev and Ising limits in the same material family.

Our experiment was motivated by a survey of the average Curie-Weiss temperature (Θ_{CW}^{avg}) and the antiferromagnetic (AFM) or spin-glass transition temperatures (T_N/T_g) of the two-dimensional (2D) iridium-, rhodium-, and ruthenium-based Kitaev materials (Fig. 1A and table S1). These compounds can be categorized into two groups. The first-generation Kitaev magnets include α-Li_2IrO_3, Na_2IrO_3, Li_2RhO_3, and α-$RuCl_3$, synthesized by conventional solid-state methods (*11*–*19*). The second-generation materials, such as $H_3LiIr_2O_6$, $Cu_3NaIr_2O_6$, and $Ag_3LiIr_2O_6$, have been synthesized recently by exchanging the interlayer alkali (Li^+ and Na^+) in the first-generation compounds with H^+, Cu^+, and Ag^+ using topochemical reactions (*20*–*26*). Both the first- and second-generation iridates appear in the same region of the phase diagram in Fig. 1A. The 4*d* systems, namely, Li_2RhO_3 and α-$RuCl_3$, appear to be shifted horizontally but not vertically from the iridate block. Despite theoretical predictions of diverse magnetic phases (*27*, *28*), it seems that all 2D Kitaev materials studied so far aggregate in the same region of the phase diagram with $T_N \leq 15$ K and a $J_{\text{eff}} = \frac{1}{2}$ state. This observation prompted us to experimentally investigate the possibility of tuning the local spin-orbital state and the magnetic ground state in the same material family.

We focused on rhodate (4*d*) systems where the SOC is weaker than in the iridate (5*d*) systems, and Δ_T has a better chance to compete with λ_{SOC}. Evidence of such competition can be found in earlier density functional theory (DFT) studies of the honeycomb rhodates, where a high sensitivity of the magnetic ground state to structural parameters has been reported (*18*, *29*). To enhance Δ_T, we replaced the Li atoms between the honeycomb layers of Li_2RhO_3 with Ag atoms and synthesized $Ag_3LiRh_2O_6$ topochemically (Fig. 1B). The change of interlayer bonds leads to a trigonal compression along the local C_3 axis (Fig. 1B). Using crystallographic refinement (fig. S1 and tables S2 and S3), we determined the bond angles within the local octahedral (O_h) environments of both compounds and quantified the trigonal distortion by calculating the bond angle variance (*9*) $\sigma = \sqrt{\sum_{i=1}^{12} (\theta - \theta_0)^2/(m-1)}$, where $m = 12$ and $\theta_0 = 90^\circ$. In an ideal octahedron, $\sigma = 0$. In $Ag_3LiRh_2O_6$, we found $\sigma = 6.1(1)^\circ$, nearly twice the $\sigma = 3.1(1)^\circ$ in Li_2RhO_3. It has been noted in earlier theoretical works (*7*, *8*) that a trigonal distortion can reconstruct the spin-orbital states and lead to new magnetic regimes; however, it has also been noted that such a regime may not be accessible in iridate materials due to the overwhelmingly strong SOC. As shown in Fig. 1A, we induced such a change of regime between Li_2RhO_3 and $Ag_3LiRh_2O_6$ using chemical pressure.

RESULTS

Magnetic properties

A small peak at $T_g = 6.0(5)$ K in Li_2RhO_3 with a splitting between the zero-field-cooled (ZFC) and field-cooled (FC) susceptibility

[1]Department of Physics, Boston College, Chestnut Hill, MA 02467, USA. [2]National Synchrotron Light Source II, Brookhaven National Laboratory, Upton, NY 11973, USA. [3]Laboratoire CRISMAT, ENSICAEN-CNRS UMR6508, 14050 Caen, France. [4]Laboratory for Muon Spin Spectroscopy (LMU), Paul Scherrer Institute (PSI), CH-5232 Villigen, Switzerland. [5]Advanced Photon Source, Argonne National Laboratory, Argonne, IL 60439, USA.
*Corresponding author. Email: fazel.tafti@bc.edu

data [$\chi(T)$ in Fig. 2A] confirms the spin-glass transition as reported in earlier works (*18*, *30*, *31*). In stark contrast, $Ag_3LiRh_2O_6$ exhibits a robust AFM order with a pronounced peak in $\chi(T)$ and without ZFC/FC splitting (Fig. 2B). The small difference between the ZFC and FC curves at low temperatures is due to a small amount of stacking faults, which are carefully analyzed in fig. S2. A Curie-Weiss analysis in Fig. 2B yields an effective moment of 1.82 μ_B and a Θ_{CW}^{avg} = 42.9 K, consistent with a prior report (*32*). A positive Θ_{CW}^{avg} despite an AFM order suggests that $\chi(T)$ must be highly anisotropic, which is the case in materials with A-type or C-type AFM order.

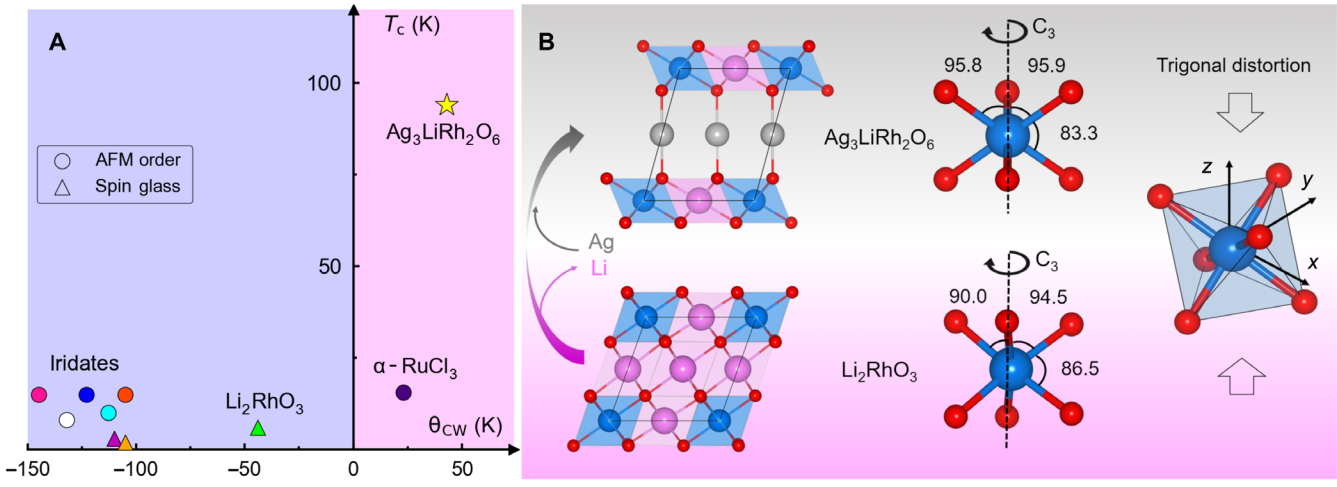

Fig. 1. Phase diagram. (**A**) Critical temperature (T_c) plotted against the Curie-Weiss temperature (Θ_{CW}^{avg}) using the data in table S1 for polycrystalline 2D Kitaev materials. Circles and triangles represent AFM and spin-glass transitions, respectively. The iridate materials are (from left to right) $Cu_3LiIr_2O_6$, $Ag_3LiIr_2O_6$, Na_2IrO^3, $Cu_3NaIr_2O_6$, Cu_2IrO_3, $H_3LiIr_2O_6$, and α-Li_2IrO_3. (**B**) Structural relationship between the first- and second-generation Kitaev systems, Li_2RhO_3 and $Ag_3LiRh_2O_6$, with enhanced trigonal distortion in the latter, as evidenced by the change of bond angles after cation exchange.

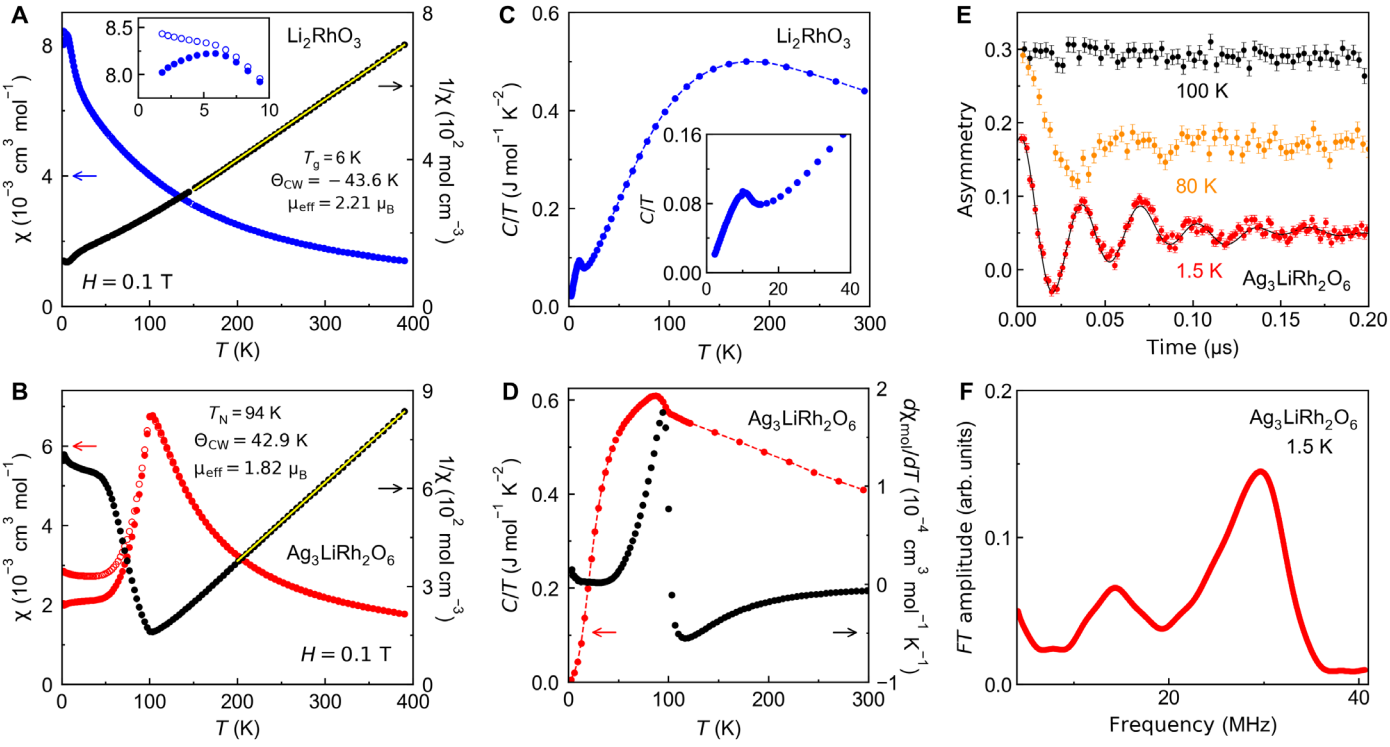

Fig. 2. Magnetic characterization. Magnetic susceptibility plotted as a function of temperature and Curie-Weiss analysis presented in (**A**) Li_2RhO_3 (blue) and (**B**) $Ag_3LiRh_2O_6$ (red). The ZFC and FC data are shown as full and empty symbols, respectively. Heat capacity as a function of temperature in (**C**) Li_2RhO_3 and (**D**) $Ag_3LiRh_2O_6$. The black circles in (**D**) show the derivative of magnetic susceptibility with respect to temperature. (**E**) μSR asymmetry plotted as a function of time in $Ag_3LiRh_2O_6$. For clarity, the curves at 100 and 80 K are offset with respect to the 1.5 K spectrum. The solid line is a fit to a Bessel function (see the Supplementary Materials for details). (**F**) Fourier transform of the μSR spectrum at 1.5 K showing two frequency components.

For example, $Na_3Ni_2BiO_6$ has a C-type AFM order [AFM intralayer and ferromagnetic (FM) interlayer] with $T_N = 10.4$ K and $\Theta_{CW}^{avg} = 13.3$ K (*33*).

Both the spin-glass transition in Li_2RhO_3 and the AFM transition in $Ag_3LiRh_2O_6$ are marked by peaks in the heat capacity in Fig. 2 (C and D). The heat capacity peak of $Ag_3LiRh_2O_6$ is visible despite the large phonon background at high temperatures, confirming a robust AFM order. We report $T_N = 94(3)$ K using the peak in $d\chi/dT$, which is close to the peak in the heat capacity (Fig. 2D). T_N in $Ag_3LiRh_2O_6$ is nearly an order of magnitude larger than the transition temperature in any other 2D Kitaev material to date.

To obtain information about the local field within the magnetically ordered state of $Ag_3LiRh_2O_6$, we turned to muon spin relaxation (μSR) experiments. In Fig. 2E, the time-dependent μSR asymmetry curves in zero applied magnetic field show the appearance of spontaneous oscillations below 100 K, confirming the long-range magnetic order. The asymmetry spectrum at 1.5 K fits to a modified zeroth-order Bessel function (*34*), with the form of the fitting function indicating noncollinear incommensurate magnetic ordering (see the Supplementary Materials for details). As shown in Fig. 2F, the Fourier transform of the 1.5 K spectrum shows two peaks at 12 and 31 MHz, which we have modeled using a two-component expression. Each component has a distribution of local fields between a B_{min} and B_{max}, indicating incommensurate ordering (table S4). The center of distribution $(B_{min} + B_{max})/2$ is shifted from zero, indicating a noncollinear order (*34*). The dominant frequency of 31 MHz in Fig. 2F corresponds to a maximum internal field of 0.231 T at the muon stopping site (using $\omega = \gamma_\mu B$ with the muon gyromagnetic ratio $\gamma_\mu = 851.6$ Mrad s^{-1} T^{-1}), which is an order of magnitude larger than the internal field of 0.015 T extracted from μSR in Li_2RhO_3 (*31*). The marked change of magnetism between Li_2RhO_3 and $Ag_3LiRh_2O_6$ in response to mild trigonal distortion, with an order-of-magnitude increase in both T_N and internal field, implies a novel underlying interaction in the ground state.

Theoretical wave functions

The drastic change of magnetic behavior between Li_2RhO_3 and $Ag_3LiRh_2O_6$ originates from a fundamental change of the spin-orbital quantum state (Fig. 3). Both Li_2RhO_3 and $Ag_3LiRh_2O_6$ have Rh^{4+} in the $4d^5$ configuration, corresponding to one hole in the t_{2g} manifold. Assuming that both compounds are in the Mott insulating regime (fig. S3), their low-energy physics should be described by a Kramers doublet per Rh^{4+} ion; i.e., they are effective spin-$\frac{1}{2}$ systems. However, the nature of the Kramers doublet may be considerably different depending on the interplay between λ_{SOC} and Δ_T. We illustrate this by considering two limits: the $J_{eff} = 1/2$ limit for $\lambda_{SOC} \gg \Delta_T$ relevant to Li_2RhO_3 (Fig. 3A) and the Ising limit for $\Delta_T \gg \lambda_{SOC}$ relevant to $Ag_3LiRh_2O_6$ (Fig. 3B). The wave functions of the low-energy Kramers doublet can be found in both limits using perturbation theory. The Kramers doublet in the $J_{eff} = 1/2$ limit ($\lambda_{SOC} \gg \Delta_T$) comprises the following two states (Fig. 3A)

$$|j_{z,\uparrow}\rangle = \sqrt{\frac{2}{3}}\,|\mu_z,\uparrow\rangle + i\sqrt{\frac{1}{3}}\,|d_{z^2},s_{z\downarrow}\rangle,\quad |j_{z,\downarrow}\rangle = \sqrt{\frac{2}{3}}\,|\mu_z,\downarrow\rangle + i\sqrt{\frac{1}{3}}\,|d_{z^2},s_{z\uparrow}\rangle \tag{1}$$

where $\{|\mu_{z,\uparrow}\rangle,\ |\mu_{z,\downarrow}\rangle\}$ are defined in Eq. 2 below. The $J_{eff} = 1/2$ limit has been discussed extensively in the literature, and sizable Kitaev interactions have been proposed for materials in this limit such as the honeycomb iridates (*1*–*4*), α-$RuCl_3$ (*16*), and Li_2RhO_3 (*29*–*31*). The only difference between Eq. 1 and prior works (*4*) is that we choose the z axis to be normal to the triangular face of the octahedron (Fig. 1B) instead of pointing at the apical oxygens.

In the Ising limit ($\Delta_T \gg \lambda_{SOC}$), the trigonal distortion leads to new Kramers doublet states (Fig. 3B)

$$\begin{aligned}|\mu_{z,\uparrow}\rangle &= -i\sqrt{\frac{1}{3}}\,|d_{x^2-y^2},s_{z\uparrow}\rangle + i\sqrt{\frac{1}{6}}\,|d_{zx},s_{z\uparrow}\rangle + \sqrt{\frac{1}{3}}\,|d_{xy},s_{z\uparrow}\rangle + \sqrt{\frac{1}{6}}\,|d_{yz},s_{z\uparrow}\rangle,\\ |\mu_{z,\downarrow}\rangle &= i\sqrt{\frac{1}{3}}\,|d_{x^2-y^2},s_{z\downarrow}\rangle - i\sqrt{\frac{1}{6}}\,|d_{zx},s_{z\downarrow}\rangle + \sqrt{\frac{1}{3}}\,|d_{xy},s_{z\downarrow}\rangle + \sqrt{\frac{1}{6}}\,|d_{yz},s_{z\downarrow}\rangle\end{aligned} \tag{2}$$

Note that the states $\{|j_{z,\uparrow}\rangle,\ |j_{z,\downarrow}\rangle\}$ are not orthogonal to the states $\{|\mu_{z,\uparrow}\rangle,\ |\mu_{z,\downarrow}\rangle\}$, despite being in opposite limits.

The trigonal splitting energy scale Δ_T is known to split the sixfold degenerate t_{2g} levels (including spin degrees of freedom) into a twofold a_{1g} manifold and a fourfold e'_g manifold (Fig. 3B) (*10*).

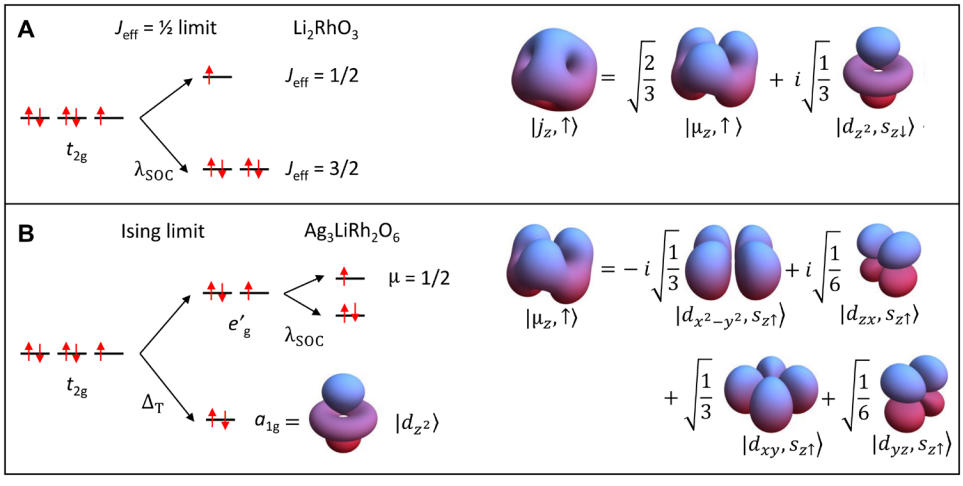

Fig. 3. Wave functions. (**A**) The $J_{eff} = 1/2$ limit, realized in Li_2RhO_3, where $\lambda_{SOC} \gg \Delta_T$. The probability density is visualized for the isospin-up wave function. (**B**) The Ising limit, realized in $Ag_3LiRh_2O_6$, where $\Delta_T \gg \lambda_{SOC}$. The probability density is visualized for the spin-up wave function. Notice the cubic and trigonal symmetries of the J_z and μ_z orbitals, respectively.

Choosing $\hat{x}$ and $\hat{y}$ directions pointing toward oxygen atoms as shown in Fig. 1B, the orbital wave functions are found to be $|d_{z^2}\rangle$ for a_{1g} (Fig. 3B) and $\{|\tau_{z,\uparrow}\rangle, |\tau_{z,\downarrow}\rangle\}$ for e_g'

$$|\tau_{z,\uparrow}\rangle \equiv \sqrt{\frac{2}{3}}|d_{x^2-y^2}\rangle - \sqrt{\frac{1}{3}}|d_{zx}\rangle,\ |\tau_{z,\downarrow}\rangle \equiv \sqrt{\frac{2}{3}}|d_{xy}\rangle + \sqrt{\frac{1}{3}}|d_{yz}\rangle \tag{3}$$

In the materials under consideration, the trigonal distortion is a compression along the $\hat{z}$ axis (Fig. 1B) that lowers the energy of the a_{1g} level (Fig. 3B). Thus, for the $4d^5$ configuration, one should focus on the fourfold e_g' manifold. Unlike in the e_g manifold, the SOC is not completely quenched in the e_g' manifold. We show, in the Supplementary Materials, that the d-orbital angular momentum operator $\vec{\mathbf{L}}$, after projection into the e_g' manifold, becomes

$$L_x \rightarrow 0, L_y \rightarrow 0, L_z \rightarrow \tau_y \tag{4}$$

where $\tau_{x,y,z}$ are the pseudospin Pauli matrices. We therefore have, in the e_g' manifold

$$\lambda_{SOC}\vec{\mathbf{L}}\cdot\vec{\mathbf{s}} \rightarrow \lambda_{SOC}L_z s_z = \lambda_{SOC}\tau_y s_z \tag{5}$$

Namely, λ_{SOC} further splits the e_g' manifold into two Kramers doublets: τ_y anti-aligned with s_z or τ_y aligned with s_z. The former doublet has a lower energy, so the latter doublet is half-filled in the $4d^5$ configuration. Last, the low-energy effective spin-$\frac{1}{2}$ states in the Ising limit are

$$|\mu_{z,\uparrow}\rangle = |\tau_y = +1, s_{z,\uparrow}\rangle,\ |\mu_{z,\downarrow}\rangle = |\tau_y = -1, s_{z,\downarrow}\rangle \tag{6}$$

which are nothing but the states written in Eq. 2 and illustrated in Fig. 3B.

The exchange couplings for the effective μ spins are expected to have the Ising anisotropy (easy-axis along the $\hat{z}$ direction). To understand its origin, one may consider exchange interactions like $J\vec{\mathbf{S}}_i\cdot\vec{\mathbf{S}}_j$ between two Rh sites i, j in the absence of the spin-orbit interaction. After λ_{SOC} is turned on, the $J\vec{\mathbf{S}}_i\cdot\vec{\mathbf{S}}_j$ needs to be projected onto the Kramers doublet $\{|\mu_{z,\uparrow}\rangle, |\mu_{z,\downarrow}\rangle\}$ at low energies. Only the term $JS_{i,z}S_{j,z}$ survives after the projection. In addition, the g factor of the effective μ spins in a magnetic field is also expected to be highly anisotropic. For example, the effective μ spins do not couple with a magnetic field along the $\hat{x}$ (or $\hat{y}$) axis in a linear fashion in this limit. A direct measurement of the magnetic response with respect to the field direction is not possible at this stage because single crystals of $Ag_3LiRh_2O_6$ are not available. However, indirect evidence of such anisotropic interactions may be the positive Curie-Weiss temperature in polycrystalline samples of $Ag_3LiRh_2O_6$ (Fig. 2B) that indicates FM interactions despite the AFM ordering. Such a behavior has been reported in $Na_3Ni_2BiO_6$ and attributed to a C-type AFM order where the coupling within the layers is AFM and between the layers is FM (*33*).

Spectroscopic evidence

We provide spectroscopic confirmation of the above picture by measuring the branching ratio using x-ray absorption spectroscopy (XAS). Figure 4A shows the XAS data from a Li_2RhO_3 sample with the Rh L_3 and L_2 edges near 3.00 and 3.15 keV, respectively. The branching ratio, BR = $I(L_3)/I(L_2)$ = 3.17(1), is evaluated by dividing the shaded areas under the L_3 and L_2 peaks in Fig. 4A. A similar analysis in $Ag_3LiRh_2O_6$ yields BR = 2.22(1) (Fig. 4B). The branching ratio is related to the SOC through BR = $(2 + r)/(1 - r)$, where $r = \langle\mathbf{L}\cdot\mathbf{S}\rangle/n_h$, with n_h being the number of holes in the $4d$ shell (*35*, *36*). Using $n_h = 5$ for Rh^{4+}, we obtain $\langle\mathbf{L}\cdot\mathbf{S}\rangle = 1.40$ in Li_2RhO_3 and 0.34 in $Ag_3LiRh_2O_6$. This is consistent with the above theoretical picture based on $\lambda_{SOC} \gg \Delta_T$ and the J_{eff} limit in Li_2RhO_3 compared to $\Delta_T \gg \lambda_{SOC}$ and the Ising limit in $Ag_3LiRh_2O_6$.

Note that the spectroscopic value of $\langle\mathbf{L}\cdot\mathbf{S}\rangle$ is small but nonvanishing in $Ag_3LiRh_2O_6$. The fine structure of Rh L edge with a shoulder near the L_3 peak (inset of Fig. 4B) that is absent in the L_2 peak confirms a finite SOC in $Ag_3LiRh_2O_6$ (*37*). As illustrated in Fig. 3B, a weak SOC is necessary to split the e_g' levels. The fine structure of

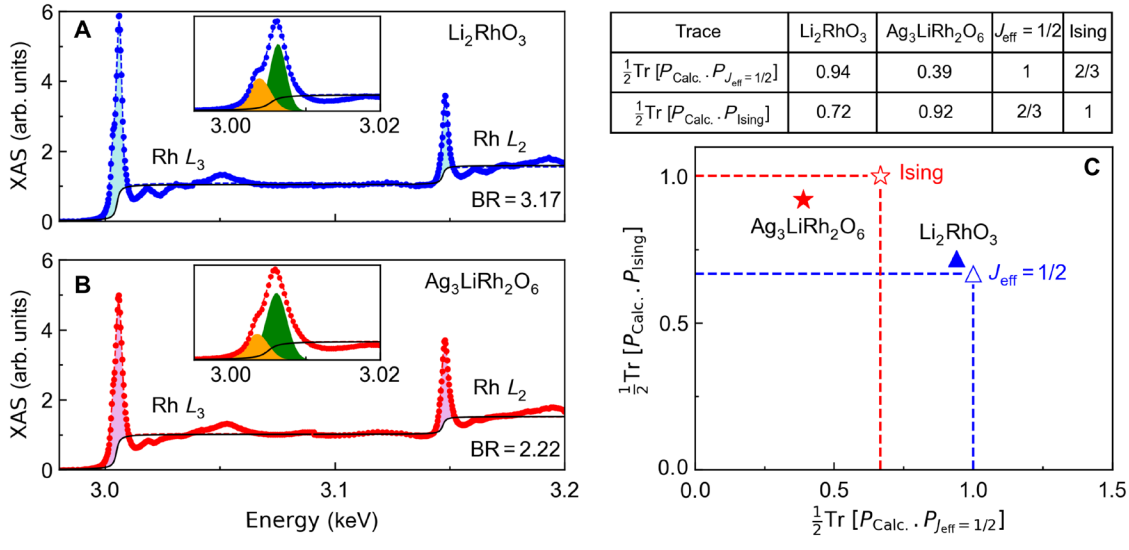

Trace	Li_2RhO_3	$Ag_3LiRh_2O_6$	J_{eff} = 1/2	Ising
$\frac{1}{2}$Tr [$P_{Calc.} \cdot P_{J_{eff}=1/2}$]	0.94	0.39	1	2/3
$\frac{1}{2}$Tr [$P_{Calc.} \cdot P_{Ising}$]	0.72	0.92	2/3	1

Fig. 4. X-ray absorption spectroscopy. (**A**) XAS data from Rh $L_{2,3}$ edges of Li_2RhO_3. The data were modeled with a step and two Gaussian functions for the L_3 edge (inset) and one Gaussian function for the L_2 edge. (**B**) Similar data and fits for the Rh $L_{2,3}$ edges of $Ag_3LiRh_2O_6$. (**C**) Theoretically calculated traces of projector products are tabulated and plotted for both the ideal limits (empty symbols) and real materials (full symbols).

the Rh L_3 edge can be fitted to two Gaussian curves in both Li_2RhO_3 and $Ag_3LiRh_2O_6$ (insets of Fig. 4, A and B). A higher ratio between the two Gaussian areas in $Ag_3LiRh_2O_6$ (2.42) than in Li_2RhO_3 (1.53) is consistent with a weaker SOC in the former. Supporting information about the Ag L edge is provided in fig. S4 to confirm the Ag^+ oxidation state (*38*, *39*).

DISCUSSION

We have demonstrated that a competition between SOC and trigonal distortion could tune a honeycomb structure between the Kitaev ($J_{eff} = \frac{1}{2}$) and Ising ($\mu = \frac{1}{2}$) limits. Our magnetization, μSR, and XAS data suggest that Li_2RhO_3 is closer to the J_{eff} limit, whereas $Ag_3LiRh_2O_6$ is closer to the Ising limit. We calculated the ideal wave functions and visualized them in Fig. 3. However, a realistic material is generally situated on a spectrum between these two ideal limits. For example, minor lattice distortions (e.g., monoclinic) can further break the trigonal point group symmetry and perturb the ideal wave function.

To make our theoretical discussion more realistic, we calculated the band structure of Li_2RhO_3 and $Ag_3LiRh_2O_6$ from first principles and obtained a real-space tight-binding model for each compound. Details of the electronic structure calculations in the presence of Hubbard-U, SOC, and zigzag magnetic ordering are presented in figs. S5 and S6 and table S5. The full orbital content of the energy eigenstates was characterized using a combination of Quantum Espresso and Wannier90 software (*40*–*42*). This allowed us to quantitatively investigate the regimes being realized in Li_2RhO_3 and $Ag_3LiRh_2O_6$. Specifically, given a Kramers doublet $|\psi_1\rangle$ and $|\psi_2\rangle$, we defined the projectors

$$P_\psi \equiv |\psi_1\rangle\langle\psi_1| + |\psi_2\rangle\langle\psi_2| \quad (7)$$

For example, $P_{Jeff=1/2}$ and P_{Ising} are projectors defined using the Kramers doublets in the J_{eff} = 1/2 limit (Eq. 1) and the Ising limit (Eq. 2), respectively. We then compute the traces $\frac{1}{2}\mathrm{Tr}[P_{calc.} \cdot P_{J_{eff}=1/2}]$ and $\frac{1}{2}\mathrm{Tr}[P_{calc.} \cdot P_{Ising}]$. The results are tabulated and visualized in Fig. 4C. These traces would be unity if the calculated system was in the ideal J_{eff} or Ising limit. Figure 4C locates Li_2RhO_3 and $Ag_3LiRh_2O_6$ in the vicinity of the J_{eff} = 1/2 and Ising (μ = 1/2) limits, respectively.

Our combined experimental and theoretical results show how to change the fabric of spin-orbit coupled states and markedly change the magnetic behavior of the Kitaev materials. Despite theoretical proposals for a diverse global phase diagram, the current Kitaev systems are all in the J_{eff} limit (*1*–*5*, *14*, *16*, *43*–*45*). Finding an outlier, such as $Ag_3LiRh_2O_6$, in the phase diagram (Fig. 1A) provides the first glimpse at the diversity of magnetic phases that can be engineered using topochemical methods. Specifically, the interplay between the Kitaev and Ising limits will be a fruitful venue to search for novel noncollinear magnetic orders beyond the familiar Kitaev-Heisenberg paradigm.

MATERIALS AND METHODS

Material synthesis

Similar to other second-generation Kitaev magnets, $Ag_3LiRh_2O_6$ is a metastable compound. It is synthesized through a topotactic cation-exchange reaction under mild conditions from the first-generation parent compound Li_2RhO_3.

$$2Li_2RhO_3 + 3AgNO_3 \longrightarrow Ag_3LiRh_2O_6 + 3LiNO_3 \quad (8)$$

Li_2RhO_3 was synthesized following prior published works (*30*, *31*). To perform the topotactic exchange reaction, Li_2RhO_3 and $AgNO_3$ powders were mixed and heated to 350°C for 1 week. The excess $AgNO_3$ was removed with deionized water.

Characterizations

Powder x-ray diffraction was performed using a Bruker D8 ECO instrument in the Bragg-Brentano geometry, using a copper source (Cu-K_α) and a LYNXEYE XE 1D energy-dispersive detector. The FullProf suite was used for the Rietveld analysis (*46*). Peak shapes were modeled with the Thompson-Cox-Hastings pseudo-Voigt profile convoluted with axial divergence asymmetry. Magnetization was measured using a Quantum Design MPMS3 with the powder sample mounted on a low-background brass holder. Both the electrical resistivity (four-probe technique) and heat capacity (relaxation time method) were measured on a pressed pellet using the Quantum Design PPMS Dynacool. Electron diffraction, high-angle annular dark-field scanning transmission electron microscopy (STEM), and annular bright-field STEM were performed using an aberration double-corrected JEM ARM200F microscope operated at 200 kV and equipped with a CENTURIOEDX detector, Orius Gatan charge-coupled device camera, and GIF Quantum spectrometer (*47*–*49*). The μSR measurements were performed in a continuous-flow ^{4}He evaporation cryostat ($T \geq 1.5$ K) at the general purpose surface-muon instrument (*50*) at the Paul Scherrer Institute, and the data were analyzed using the Musrfit program (*51*). A pressed disk of $Ag_3LiRh_2O_6$ with diameter 12 mm and thickness 1.2 mm was wrapped in 25-μm silver foil and suspended in the muon beam to minimize the contribution from muons implanted in a sample holder or in the cryostat walls.

First-principles calculations

The electronic structures were computed using the open-source code Quantum Espresso (*40*, *41*) with the experimental crystallographic information as the input. The calculation included SOC and zigzag magnetic ordering for both compounds, and the fully gapped states were achieved using a DFT + U method (*52*). To stabilize the noncollinear magnetic calculation, we used the norm-conserving pseudopotentials from PseudoDojo (*53*). For convergence reasons, we implemented the Perdew-Zunger functional in the calculation of $Ag_3LiRh_2O_6$, while leaving the default Perdew-Burke-Ernzerhof functional for Li_2RhO_3. To compare with the previous report of the insulating states in chemical formula Li_2RhO_3 (LRO) (*18*), we fixed the Hund's coupling to J = 0.7 eV and tuned the Hubbard-U from 1 to 4 eV. Our results were consistent with the prior work. The real-space tight-binding functions (involving the Rh-4*d* and O-2*p* orbitals as well as Ag-4*d* orbitals for $Ag_3LiRh_2O_6$) were derived from the band structure using maximally localized Wannier states implemented by the Wannier90 software (*42*). From here, tight-binding models for a single RhO_6 cluster were constructed on the basis of the obtained real-space hopping parameters. The eigenstates of such a RhO_6 cluster were used to compute $\langle \mathbf{L} \cdot \mathbf{S} \rangle$ and the traces in Fig. 4.

X-ray absorption spectroscopy

X-ray absorption near-edge structure data at Rh and Ag $L_{2,3}$ edges were collected at tender energy beamline 8-BM of the National Synchrotron Light Source II and at beamline 4-ID-D of the Advanced

Photon Source, respectively. The Rh $L_{2,3}$ data were collected in total electron yield mode using powder samples in a helium gas environment. The Ag $L_{2,3}$ data were collected in partial fluorescence yield (PFY) mode with powder samples in vacuum. Silicon and nickel mirrors together with detuning of the second Si(111) monochromator crystal were used to reject high-energy harmonics. The PFY data were corrected for self-absorption (*54*).

SUPPLEMENTARY MATERIALS

Supplementary material for this article is available at https://science.org/doi/10.1126/sciadv.abl5671

REFERENCES AND NOTES

1. H. Takagi, T. Takayama, G. Jackeli, G. Khaliullin, S. E. Nagler, Concept and realization of Kitaev quantum spin liquids. *Nat. Rev. Phys.* **1**, 264–280 (2019).
2. J. Knolle, R. Moessner, A field guide to spin liquids. *Annu. Rev. Condens. Matter Phys.* **10**, 451–472 (2019).
3. J. Chaloupka, G. Jackeli, G. Khaliullin, Kitaev-Heisenberg model on a honeycomb lattice: Possible exotic phases in iridium oxides A_2IrO_3. *Phys. Rev. Lett.* **105**, 027204 (2010).
4. G. Jackeli, G. Khaliullin, Mott insulators in the strong spin-orbit coupling limit: From Heisenberg to a quantum compass and Kitaev models. *Phys. Rev. Lett.* **102**, 017205 (2009).
5. B. J. Kim, H. Jin, S. J. Moon, J.-Y. Kim, B.-G. Park, C. S. Leem, J. Yu, T. W. Noh, C. Kim, S.-J. Oh, J.-H. Park, V. Durairaj, G. Cao, E. Rotenberg, Novel $J_{\text{eff}} = 1/2$ Mott state induced by relativistic spin-orbit coupling in Sr_2IrO_4. *Phys. Rev. Lett.* **101**, 076402 (2008).
6. A. Kitaev, Anyons in an exactly solved model and beyond. *Ann. Phys.* **321**, 2–111 (2006).
7. G. Khaliullin, Orbital order and fluctuations in Mott insulators. *Prog. Theor. Phys. Suppl.* **160**, 155–202 (2005).
8. S. Bhattacharjee, S.-S. Lee, Y. B. Kim, Spin–orbital locking, emergent pseudo-spin and magnetic order in honeycomb lattice iridates. *New J. Phys.* **14**, 073015 (2012).
9. Y. Haraguchi, H. A. Katori, Strong antiferromagnetic interaction owing to a large trigonal distortion in the spin-orbit-coupled honeycomb lattice iridate $CdIrO_3$. *Phys. Rev. Mater.* **4**, 044401 (2020).
10. P. A. Joy, S. Vasudevan, Magnetism in the layered transition-metal thiophosphates MPS_3 (M = Mn, Fe, and Ni). *Phys. Rev. B* **46**, 5425–5433 (1992).
11. Y. Singh, S. Manni, J. Reuther, T. Berlijn, R. Thomale, W. Ku, S. Trebst, P. Gegenwart, Relevance of the Heisenberg-Kitaev model for the honeycomb lattice iridates A_2IrO_3. *Phys. Rev. Lett.* **108**, 127203 (2012).
12. K. Mehlawat, A. Thamizhavel, Y. Singh, Heat capacity evidence for proximity to the Kitaev quantum spin liquid in A_2IrO_3 (A = Na, Li). *Phys. Rev. B* **95**, 144406 (2017).
13. Y. Singh, P. Gegenwart, Antiferromagnetic Mott insulating state in single crystals of the honeycomb lattice material Na_2IrO_3. *Phys. Rev. B* **82**, 064412 (2010).
14. K. W. Plumb, J. P. Clancy, L. J. Sandilands, V. V. Shankar, Y. F. Hu, K. S. Burch, H.-Y. Kee, Y.-J. Kim, α-$RuCl_3$: A spin-orbit assisted Mott insulator on a honeycomb lattice. *Phys. Rev. B* **90**, 041112 (2014).
15. Y. Kobayashi, T. Okada, K. Asai, M. Katada, H. Sano, F. Ambe, Moessbauer spectroscopy and magnetization studies of α- and β-ruthenium trichloride. *Inorg. Chem.* **31**, 4570–4574 (1992).
16. A. Koitzsch, C. Habenicht, E. Müller, M. Knupfer, B. Büchner, H. Kandpal, J. van den Brink, D. Nowak, A. Isaeva, T. Doert, J_{eff} description of the honeycomb Mott insulator α-$RuCl_3$. *Phys. Rev. Lett.* **117**, 126403 (2016).
17. A. Banerjee, C. A. Bridges, J.-Q. Yan, A. A. Aczel, L. Li, M. B. Stone, G. E. Granroth, M. D. Lumsden, Y. Yiu, J. Knolle, S. Bhattacharjee, D. L. Kovrizhin, R. Moessner, D. A. Tennant, D. G. Mandrus, S. E. Nagler, Proximate Kitaev quantum spin liquid behaviour in a honeycomb magnet. *Nat. Mater.* **15**, 733–740 (2016).
18. I. I. Mazin, S. Manni, K. Foyevtsova, H. O. Jeschke, P. Gegenwart, R. Valentí, Origin of the insulating state in honeycomb iridates and rhodates. *Phys. Rev. B* **88**, 035115 (2013).
19. V. Todorova, M. Jansen, Synthesis, structural characterization and physical properties of a new member of ternary lithium layered compounds—Li_2RhO_3. *Z. Anorg. Allg. Chem.* **637**, 37–40 (2011).
20. J. H. Roudebush, K. A. Ross, R. J. Cava, Iridium containing honeycomb delafossites by topotactic cation exchange. *Dalton Trans.* **45**, 8783–8789 (2016).
21. M. Abramchuk, C. Ozsoy-Keskinbora, J. W. Krizan, K. R. Metz, D. C. Bell, F. Tafti, Cu_2IrO_3: A new magnetically frustrated honeycomb iridate. *J. Am. Chem. Soc.* **139**, 15371–15376 (2017).
22. F. Bahrami, E. M. Kenney, C. Wang, A. Berlie, O. I. Lebedev, M. J. Graf, F. Tafti, Effect of structural disorder on the Kitaev magnet $Ag_3LiIr_2O_6$. *Phys. Rev. B* **103**, 094427 (2021).
23. E. M. Kenney, C. U. Segre, W. Lafargue-Dit-Hauret, O. I. Lebedev, M. Abramchuk, A. Berlie, S. P. Cottrell, G. Simutis, F. Bahrami, N. E. Mordvinova, G. Fabbris, J. L. McChesney, D. Haskel, X. Rocquefelte, M. J. Graf, F. Tafti, Coexistence of static and dynamic magnetism in the Kitaev spin liquid material Cu_2IrO_3. *Phys. Rev. B* **100**, 094418 (2019).
24. S. K. Takahashi, J. Wang, A. Arsenault, T. Imai, M. Abramchuk, F. Tafti, P. M. Singer, Spin excitations of a proximate Kitaev quantum spin liquid realized in Cu_2IrO_3. *Phys. Rev. X* **9**, 031047 (2019).
25. F. Bahrami, W. Lafargue-Dit-Hauret, O. I. Lebedev, R. Movshovich, H.-Y. Yang, D. Broido, X. Rocquefelte, F. Tafti, Thermodynamic evidence of proximity to a Kitaev spin liquid in $Ag_3LiIr_2O_6$. *Phys. Rev. Lett.* **123**, 237203 (2019).
26. K. Kitagawa, T. Takayama, Y. Matsumoto, A. Kato, R. Takano, Y. Kishimoto, S. Bette, R. Dinnebier, G. Jackeli, H. Takagi, A spin–orbital-entangled quantum liquid on a honeycomb lattice. *Nature* **554**, 341–345 (2018).
27. J. Rusnačko, D. Gotfryd, J. Chaloupka, Kitaev-like honeycomb magnets: Global phase behavior and emergent effective models. *Phys. Rev. B* **99**, 064425 (2019).
28. J. G. Rau, E. K.-H. Lee, H.-Y. Kee, Generic spin model for the honeycomb iridates beyond the Kitaev limit. *Phys. Rev. Lett.* **112**, 077204 (2014).
29. V. M. Katukuri, S. Nishimoto, I. Rousochatzakis, H. Stoll, J. van den Brink, L. Hozoi, Strong magnetic frustration and anti-site disorder causing spin-glass behavior in honeycomb Li_2RhO_3. *Sci. Rep.* **5**, 14718 (2015).
30. Y. Luo, C. Cao, B. Si, Y. Li, J. Bao, H. Guo, X. Yang, C. Shen, C. Feng, J. Dai, G. Cao, Z.-a. Xu, Li_2RhO_3: A spin-glassy relativistic Mott insulator. *Phys. Rev. B* **87**, 161121 (2013).
31. P. Khuntia, S. Manni, F. R. Foronda, T. Lancaster, S. J. Blundell, P. Gegenwart, M. Baenitz, Local magnetism and spin dynamics of the frustrated honeycomb rhodate Li_2RhO_3. *Phys. Rev. B* **96**, 094432 (2017).
32. V. Todorova, A. Leineweber, L. Kienle, V. Duppel, M. Jansen, On $AgRhO_2$, and the new quaternary delafossites $AgLi_{1/3}M_{2/3}O_2$, syntheses and analyses of real structures. *J. Solid State Chem.* **184**, 1112–1119 (2011).
33. E. M. Seibel, J. H. Roudebush, H. Wu, Q. Huang, M. N. Ali, H. Ji, R. J. Cava, Structure and magnetic properties of the α-$NaFeO_2$-type honeycomb compound $Na_3Ni_2BiO_6$. *Inorg. Chem.* **52**, 13605–13611 (2013).
34. A. Amato, P. Dalmas de Réotier, D. Andreica, A. Yaouanc, A. Suter, G. Lapertot, I. M. Pop, E. Morenzoni, P. Bonfà, F. Bernardini, R. De Renzi, Understanding the μSR spectra of MnSi without magnetic polarons. *Phys. Rev. B* **89**, 184425 (2014).
35. G. van der Laan, B. T. Thole, Local probe for spin-orbit interaction. *Phys. Rev. Lett.* **60**, 1977–1980 (1988).
36. M. A. Laguna-Marco, D. Haskel, N. Souza-Neto, J. C. Lang, V. V. Krishnamurthy, S. Chikara, G. Cao, M. van Veenendaal, Orbital magnetism and spin-orbit effects in the electronic structure of $BaIrO_3$. *Phys. Rev. Lett.* **105**, 216407 (2010).
37. F. M. F. de Groot, Z. W. Hu, M. F. Lopez, G. Kaindl, F. Guillot, M. Tronc, Differences between L_3 and L_2 x-ray absorption spectra of transition metal compounds. *J. Chem. Phys.* **101**, 6570–6576 (1994).
38. A. V. Kolobov, A. Rogalev, F. Wilhelm, N. Jaouen, T. Shima, J. Tominaga, Thermal decomposition of a thin AgO_x layer generating optical near-field. *Appl. Phys. Lett.* **84**, 1641–1643 (2004).
39. P. Behrens, S. Aßmann, U. Bilow, C. Linke, M. Jansen, Electronic structure of silver oxides investigated by AgL XANES spectroscopy. *Z. Anorg. Allg. Chem.* **625**, 111–116 (1999).
40. P. Giannozzi, S. Baroni, N. Bonini, M. Calandra, R. Car, C. Cavazzoni, D. Ceresoli, G. L. Chiarotti, M. Cococcioni, I. Dabo, A. D. Corso, S. de Gironcoli, S. Fabris, G. Fratesi, R. Gebauer, U. Gerstmann, C. Gougoussis, A. Kokalj, M. Lazzeri, L. Martin-Samos, N. Marzari, F. Mauri, R. Mazzarello, S. Paolini, A. Pasquarello, L. Paulatto, C. Sbraccia, S. Scandolo, G. Sclauzero, A. P. Seitsonen, A. Smogunov, P. Umari, R. M. Wentzcovitch, Quantum espresso: A modular and open-source software project for quantum simulations of materials. *J. Phys. Condens. Matter* **21**, 395502 (2009).
41. P. Giannozzi, O. Andreussi, T. Brumme, O. Bunau, M. B. Nardelli, M. Calandra, R. Car, C. Cavazzoni, D. Ceresoli, M. Cococcioni, N. Colonna, I. Carnimeo, A. Dal Corso, S. de Gironcoli, P. Delugas, R. A. Di Stasio Jr., A. Ferretti, A. Floris, G. Fratesi, G. Fugallo, R. Gebauer, U. Gerstmann, F. Giustino, T. Gorni, J. Jia, M. Kawamura, H.-Y. Ko, A. Kokalj, E. Küçükbenli, M. Lazzeri, M. Marsili, N. Marzari, F. Mauri, N. L. Nguyen, H.-V. Nguyen, A. Otero-de-la-Roza, L. Paulatto, S. Poncé, D. Rocca, R. Sabatini, B. Santra, M. Schlipf, A. P. Seitsonen, A. Smogunov, I. Timrov, T. Thonhauser, P. Umari, N. Vast, X. Wu, S. Baroni, Advanced capabilities for materials modelling with quantum ESPRESSO. *J. Phys. Condens. Matter* **29**, 465901 (2017).
42. G. Pizzi, V. Vitale, R. Arita, S. Blügel, F. Freimuth, G. Géranton, M. Gibertini, D. Gresch, C. Johnson, T. Koretsune, J. Ibañez-Azpiroz, H. Lee, J.-M. Lihm, D. Marchand, A. Marrazzo, Y. Mokrousov, J. I. Mustafa, Y. Nohara, Y. Nomura, L. Paulatto, S. Poncé, T. Ponweiser, J. Qiao, F. Thöle, S. S. Tsirkin, M. Wierzbowska, N. Marzari, D. Vanderbilt, I. Souza, A. A. Mostofi, J. R. Yates, Wannier90 as a community code: New features and applications. *J. Phys. Condens. Matter* **32**, 165902 (2020).
43. J. A. Sears, L. E. Chern, S. Kim, P. J. Bereciartua, S. Francoual, Y. B. Kim, Y.-J. Kim, Ferromagnetic Kitaev interaction and the origin of large magnetic anisotropy in α-$RuCl_3$. *Nat. Phys.* **16**, 837–840 (2020).

44. H. Gretarsson, J. P. Clancy, X. Liu, J. P. Hill, E. Bozin, Y. Singh, S. Manni, P. Gegenwart, J. Kim, A. H. Said, D. Casa, T. Gog, M. H. Upton, H.-S. Kim, J. Yu, V. M. Katukuri, L. Hozoi, J. van den Brink, Y.-J. Kim, Crystal-field splitting and correlation effect on the electronic structure of A_2IrO_3. *Phys. Rev. Lett.* **110**, 076402 (2013).
45. J. P. Clancy, H. Gretarsson, J. A. Sears, Y. Singh, S. Desgreniers, K. Mehlawat, S. Layek, G. K. Rozenberg, Y. Ding, M. H. Upton, D. Casa, N. Chen, J. Im, Y. Lee, R. Yadav, L. Hozoi, D. Efremov, J. van den Brink, Y.-J. Kim, Pressure-driven collapse of the relativistic electronic ground state in a honeycomb iridate. *npj Quantum Mater.* **3**, 35 (2018).
46. J. Rodríguez-Carvajal, Recent advances in magnetic structure determination by neutron powder diffraction. *Phys. B Condens. Matter* **192**, 55–69 (1993).
47. C. R. Houska, T. M. Smith, Least-squares analysis of x-ray diffraction line shapes with analytic functions. *J. Appl. Phys.* **52**, 748–754 (1981).
48. M. Abramchuk, O. I. Lebedev, O. Hellman, F. Bahrami, N. E. Mordvinova, J. W. Krizan, K. R. Metz, D. Broido, F. Tafti, Crystal chemistry and phonon heat capacity in quaternary honeycomb delafossites: $Cu[Li_{1/3}Sn_{2/3}]O_2$ and $Cu[Na_{1/3}Sn_{2/3}]O_2$. *Inorg. Chem.* **57**, 12709–12717 (2018).
49. O. L. Krivanek, M. F. Chisholm, V. Nicolosi, T. J. Pennycook, G. J. Corbin, N. Dellby, M. F. Murfitt, C. S. Own, Z. S. Szilagyi, M. P. Oxley, S. T. Pantelides, S. J. Pennycook, Atom-by-atom structural and chemical analysis by annular dark-field electron microscopy. *Nature* **464**, 571–574 (2010).
50. A. Amato, H. Luetkens, K. Sedlak, A. Stoykov, R. Scheuermann, M. Elender, A. Raselli, D. Graf, The new versatile general purpose surface-muon instrument (GPS) based on silicon photomultipliers for μSR measurements on a continuous-wave beam. *Rev. Sci. Instrum.* **88**, 093301 (2017).
51. A. Suter, B. M. Wojek, Musrfit: A free platform-independent framework for μSR data analysis. *Phys. Procedia* **30**, 69–73 (2012).
52. M. Cococcioni, S. de Gironcoli, Linear response approach to the calculation of the effective interaction parameters in the LDA+ U method. *Phys. Rev. B* **71**, 035105 (2005).
53. M. J. van Setten, M. Giantomassi, E. Bousquet, M. J. Verstraete, D. R. Hamann, X. Gonze, G. M. Rignanese, The PseudoDojo: Training and grading a 85 element optimized norm-conserving pseudopotential table. *Comput. Phys. Commun.* **226**, 39–54 (2018).
54. D. Haskel, Fluo: Correcting xanes for self-absorption in fluorescence measurements. Computer program and documentation (1999); https://www3.aps.anl.gov/haskel/fluo.html.

Acknowledgments: We thank R. Valenti and Y. Li for fruitful discussions. **Funding:** F.T. and F.B. acknowledge support from the NSF under grant no. DMR-1708929. Y.R. and X.H. acknowledge support from the NSF under grant no. DMR-1712128. This work is based, in part, on experiments performed at the Swiss Muon Source SμS, Paul Scherrer Institute, Villigen, Switzerland. This research used 8-BM of the National Synchrotron Light Source II, a U.S. Department of Energy (DOE) Office of Science User Facility operated for the DOE Office of Science by Brookhaven National laboratory under contract no. DE-SC0012704. Work at the Advanced Photon Source was supported by the DOE of Science, Office of Basic Energy Sciences, under award no. DE-AC02-06CH11357. **Author contributions:** F.B. synthesized the materials, performed magnetic and thermodynamic measurements, and analyzed the data. O.I.L. performed TEM experiments. X.H. and Y.R. performed theoretical calculations. Y.D., G.F., and D.H. performed XAS experiments. C.W., H.L., and M.J.G. performed μSR experiments. F.T. conceptualized the project. All authors participated in writing. **Competing interests:** The authors declare that they have no competing interests. **Data and materials availability:** All data needed to evaluate the conclusions in the paper are present in the paper and/or the Supplementary Materials and permanently archived in Materials Data Facility (DOI: 10.18126/ar66-63gd, LINK: https://doi.org/10.18126/AR66-63GD).

Submitted 22 July 2021
Accepted 1 February 2022
Published 23 March 2022
10.1126/sciadv.abl5671

ScienceAdvances

First demonstration of tuning between the Kitaev and Ising limits in a honeycomb lattice

Faranak BahramiXiaodong HuYonghua DuOleg I. LebedevChennan WangHubertus LuetkensGilberto FabbrisMichael J. GrafDaniel HaskelYing RanFazel Tafti

Sci. Adv., 8 (12), eabl5671. • DOI: 10.1126/sciadv.abl5671

Science Advances (ISSN) is published by the American Association for the Advancement of Science. 1200 New York Avenue NW, Washington, DC 20005. The title *Science Advances* is a registered trademark of AAAS.